ADVANCED MATERIALS

Supporting Information

for *Adv. Mater.*, DOI: 10.1002/adma.201906657

Magnetic Shape Memory Polymers with Integrated Multifunctional Shape Manipulation

Qiji Ze, Xiao Kuang, Shuai Wu, Janet Wong, S. Macrae Montgomery, Rundong Zhang, Joshua M. Kovitz, Fengyuan Yang, H. Jerry Qi, and Ruike Zhao**

Supporting Information

Magnetic Shape Memory Polymers with Integrated Multifunctional Shape Manipulation

Qiji Ze, Xiao Kuang, Shuai Wu, Janet Wong, S. Macrae Montgomery, Rundong Zhang, Joshua M. Kovitz, Fengyuan Yang, H. Jerry Qi, Ruike Zhao**

Supplementary Methods

Fourier transform infrared (FTIR) spectra are recorded on a Nicolet iS50 spectrometer (Thermo Fisher Scientific, Waltham, MA, USA) by averaging 32 scans of the signal at a resolution of 2 cm^{-1} in the attenuated total reflectance mode.

Shape memory tests are conducted in a "Control Force" mode on a dynamic mechanical analysis (DMA) tester (DMA850, TA Instruments, Inc., New Castle, DE, USA). Shape fixity and recovery are calculated as follows:

$$R_{\mathrm{f}} = \frac{\varepsilon^{*}}{\varepsilon_{load}} \times 100\%, \tag{S1}$$

$$R_{\mathrm{r}} = \frac{\varepsilon^{*} - \varepsilon_{rec}}{\varepsilon^{*}} \times 100\%, \tag{S2}$$

where ε_{load} is the maximum applied strain at high temperature, ε^{*} is the fixed strain after cooling and force removal, and ε_{rec} is the recovered strain.

Scanning Electron Microscopy (SEM) images are obtained by a Hitachi SU8010 SEM (Hitachi Ltd, Chiyoda, Tokyo, Japan) with a working distance of 6−8 mm and a voltage of 5 kV.

High-frequency hysteresis loops are measured to estimate the inductive heating power of the Fe_3O_4 particles within different high-frequency AC magnetic fields. The measurement setup[1] consists of a measurement coil system placed at the center of the solenoid, which generates a 60 kHz magnetic field. The schematic of the setup is shown in Figure S7a. The voltages of $e_1(t)$ and $e_2(t)$ are measured using an oscilloscope (EDUX1002A, Keysight Technologies, Inc., Santa Rosa, CA, USA). The magnetic flux density $B(t)$ and magnetic moment density $M(t)$ can be integrated using the following equations:

$$B(t) = \frac{\int e_1(t)\,dt}{nS_{coil}}, \tag{S3}$$

$$M(t)=\frac{\int e_2(t)\,dt}{\mu_0 n\varphi_m S_m},\tag{S4}$$

where n is the number of turns, S_{coil} is the cross-sectional area of the measurement coil, μ_0 is the permeability of vacuum, φ_m is the NdFeB volume fraction of the M-SMP sample, and S_m is the area of the section perpendicular to the direction of the AC magnetic field. In our measurement system, n, S_{coil}, and S_m are 5, 314.16 mm^2, and 100 mm^2, respectively. The hysteresis loops of the M-SMPs with different Fe_3O_4 loadings, under different magnetic strengths, and with different particle sizes are obtained and plotted in Figure 2e, Figure S7b, and Figure S8a, respectively.

For the Fe_3O_4 particles used in this paper, the inductive heating power mainly comes from the hysteresis loss.[2] The power density p can be calculated from the loop area and the frequency f of the magnetic field by the following equation:

$$p=f\cdot\int MdB\,.\tag{S5}$$

Recall that M is the magnetic moment density of the M-SMP, and B is the applied magnetic flux density. The calculated heating power density for the M-SMPs with different Fe_3O_4 loadings and different particle sizes under different magnetic field strengths are shown in Figure 2f and Figure 8b, respectively. The inductive heating power increases with increasing magnetic field strength and Fe_3O_4 loading, and decreasing Fe_3O_4 particle size (for tested particles sizes of 100 nm, 300 nm, and 30 μm).

Static magnetization characterizations are performed on a Vibrating Sample Magnetometer (VSM, 7400A series, Lake Shore Cryotronics, Inc., Chicago, IL, USA). The static magnetization curve of the M-SMP shown in Figure 2d is measured at room temperature. The external magnetic flux density (B) is from −1.5 T to 1.5 T with a stepwise increase at 0.1 T step^{-1}. The measured magnetic moment is divided by the sample's volume to obtain the remnant magnetic moment density (M_r). To measure the M-SMP's magnetization as a function of temperature (Figure S10), the sample is first placed in the VSM chamber and is magnetized under a magnetic field of 1.5 T at 25°C. The magnetic moment is then measured every 10°C as the temperature in the chamber gradually increases to 355°C at a heating rate of 5°C min^{-1}. The calculated M_r is then divided by its initial value at 25°C to obtain the normalized remnant magnetic moment density ($\overline{M_r}$).

Viscosity measurement: DV2TLV cone and plate viscometer with a cone spindle of CPA-52Z (Brookfield Engineering Labs Inc., Middleboro, MA, USA) is used to measure the viscosity of the M-SMPs with different particle sizes under a shear rate of 0.2 s^{-1}.

Antenna simulation and experiments: The helical antenna is molded with a 3D-printed PVA mold using an Ultimaker S5. After thermal curing of the M-SMP, the PVA mold is dissolved in water. The cured sample is softened and deformed to the shape shown in Figure S13. It is then magnetized along its height direction. The antenna is transformed and locked to the expected actuated shape and is fed by a 50 Ω coaxial probe. The antenna's return loss (S_{11}) is measured using a Vector Network Analyzer (VNA). The antenna is connected to a 50 Ω SMA connector on a 300 mm × 300 mm aluminum ground plane. After achieving the desired antenna shape using B_h and B_a, the feed pin of the SMA connector is connected to the conductive silver lines on the antenna, exciting the antenna for measurements. The bandwidths of interest during the measurement are from 0.5 GHz to 2 GHz for the cantilever-based antennas and 2 GHz to 4 GHz for the helical antenna. All antenna simulations are conducted using ANSYS Electromagnetic Suite V19.10 HFSS.

Figure S14a shows the design of a cantilever-based, morphing monopole antenna (48 mm long). It can be reprogrammed with different magnetization profiles to transform into different shapes for deployable and reconfigurable antennas. Gravity initially drives the cantilever to bend down (Down shape) upon heating in the absence of a magnetic field. With a magnetization profile oriented along its longitudinal direction, the Down shape can be actuated to the Up shape under B_a = 20 mT (Figure S14b). Figure S14c shows the antenna works as a deployable monopole antenna due to its poor impedance (S_{11} larger than the acceptable value, −10 dB)[3] in the Down shape but good S_{11} value with a resonant frequency of 0.95 GHz in the Up shape. Moreover, this deployable antenna can be altered to a reconfigurable antenna by reprogramming the M-SMP's magnetization profile. Here, the same cantilever is remagnetized to have a sinusoidal shape with a height of 24 mm under B_a = 80 mT (Figure S14d, and Video S4). Figure S10e shows the resonant frequency of this antenna shifts from 0.95 GHz (Up shape) to 1.25 GHz (sinusoidal shape), representing a 32% change, with good agreement achieved between the simulation and experimental results. The radiation pattern simulations and polar plots are similar for all these configurations (Figure S14f), which is beneficial as a reconfigurable antenna.

Finite element simulations. The complete operation of our M-SMP has three phases, which are heating phase, actuation phase, and locking phase. In this paper, the actuation phase of our M-SMPs at high temperature can be estimated by the theoretical framework from a recent work.[4] In that work, a constitutive model considering the hyperelastic behavior of the matrix and the magnetic potential of the material was developed and implemented through a user-defined element subroutine in the commercial finite element software ABAQUS, to predict the magnetic actuation of magnetic soft materials. Without considering the time-temperature-dependent behaviors of M-SMPs, the hyperelastic property at high temperature, magnetic moment density, and applied magnetic field serve as inputs to the material model. Then the deformation can be predicted as shown in Figure S11.

Energy consumption: In our system, the energy consumption came from heating, actuation, and shape locking. We estimated the energy consumption for the three operation procedures as follows.

<u>Energy consumption during heating:</u>

For heating, a 600 A current is applied to generate a 40 mT high-frequency magnetic field. The resistance of the solenoid is about 0.001 Ω and the corresponding power consumption is around 0.18 kW. For the P15-15 M-SMP, it can reach the actuation temperature (around 50ºC) after 10s heating, which corresponds to 1800 J energy. Depending on different applications, the energy consumption from heating can be reduced by increasing the heating efficiency of the M-SMP through reducing Fe_3O_4 particle size and/or increasing Fe_3O_4 particle loading.

Energy consumption during actuation:

A pair of electromagnetic coils is used for actuation. The power consumption of the coils can be estimated by considering the coil resistance (around 6 Ω) and the applied current for actuation. To actuate the M-SMP beam shown in Figure 3b at its soft state, 1 A current, which corresponds to 7 mT, can already provide reasonable shape change. In this case, the power consumption is only 6 W. In addition, by taking advantage of the fast-transforming nature of the magnetic soft material, the actuation time is less than 0.1 s, which leads to 0.6 J energy consumption during actuation.

Energy consumption during shape locking:

During shape locking, the heating magnetic field is off, and the energy consumption only comes from the actuation coils. The power consumption follows the estimation for actuation and the total energy consumption is determined by the cooling time. As discussed above, the energy consumption during actuation is very small. Also, different strategies can be adopted to reduce the cooling time and resultant energy consumption.

Supplementary Figures and Figure Captions

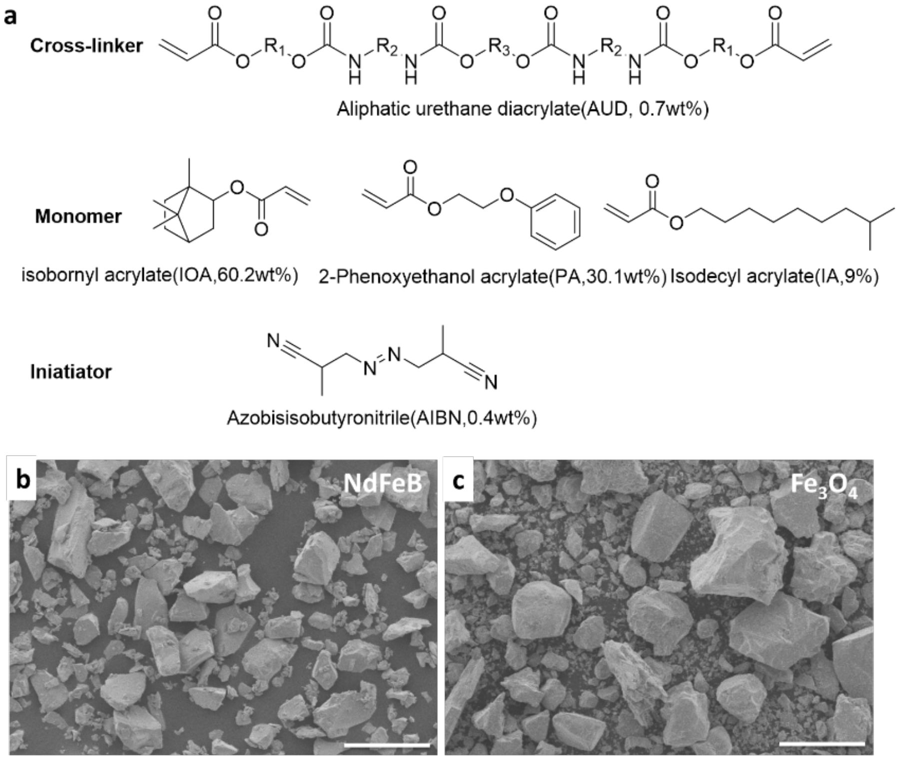

Figure S1. Resin formulation and morphology of magnetic particles. (a) Chemical structures of each component in the resin. SEM images of (b) NdFeB and (c) Fe_3O_4. Scale bars: 50 μm.

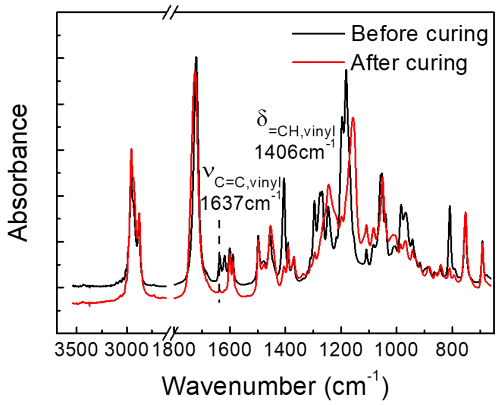

Figure S2. FTIR spectrum of polymer matrix before and after thermal curing. The band at 1637 cm^{-1} is attributed to the vinyl carbon-carbon stretching vibration, and its sharp decrease in intensity indicates the polymerization of the cross-linkers and monomers into a polymer.

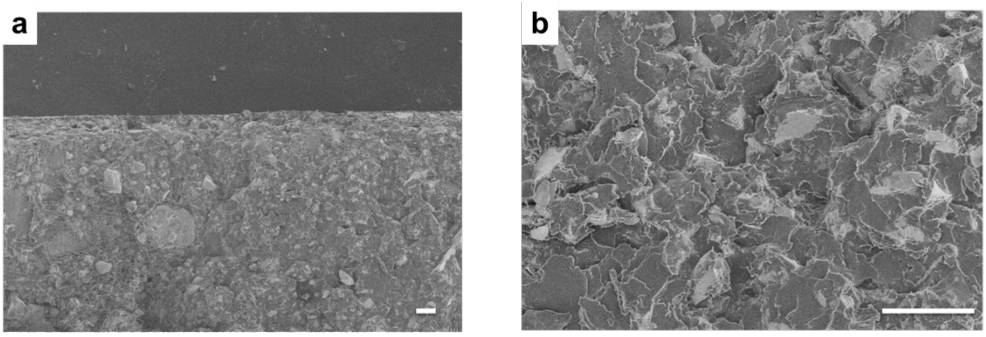

Figure S3. SEM images of M-SMP (P15-15) at two different magnifications. Scale bars: 50 μm.

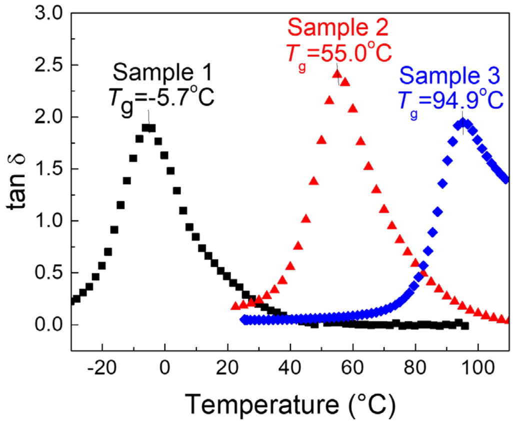

Figure S4. tan δ versus temperature curves for the SMPs with tunable T_g by adjusting the ratios of rigid and flexible acrylates.

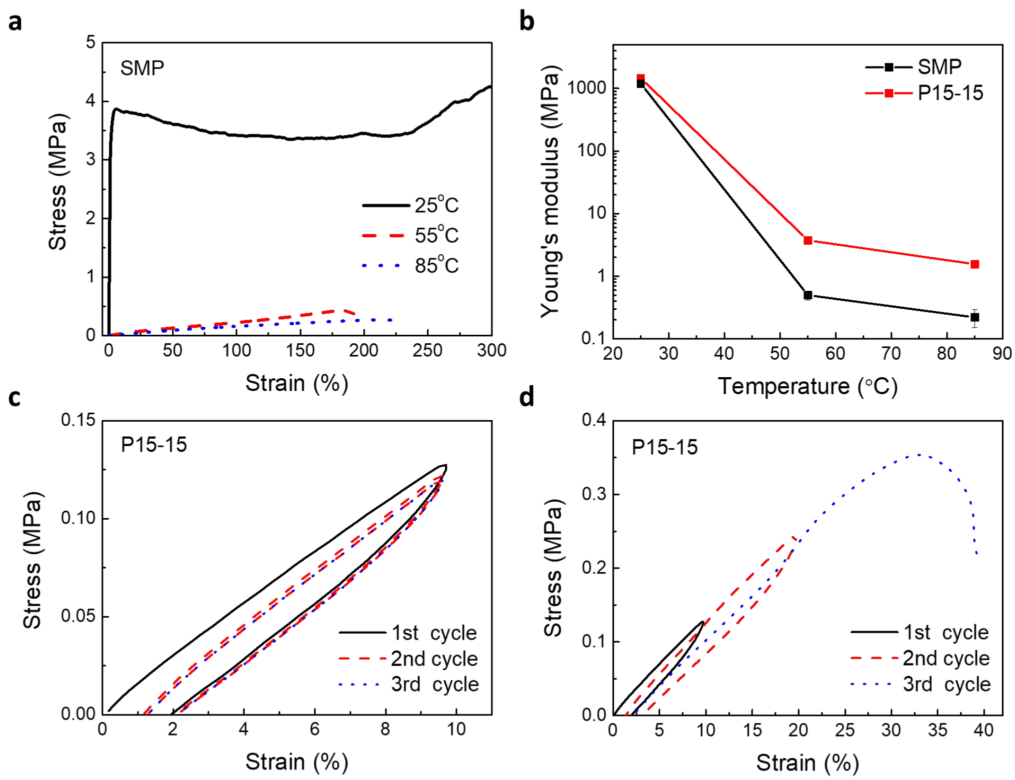

Figure S5. Mechanical properties of M-SMPs. (a) Tensile stress-strain curves of neat SMP at 25ºC, 55ºC, and 85ºC. (b) Comparison of the temperature-dependent Young's moduli for neat SMP and P15-15. (c) Cyclic tensile test of P15-15 loaded to 10% strain at 85ºC. (d) Cyclic tensile tests of P15-15 with different maximum strains. The strain rate is 0.2 min^{-1}.

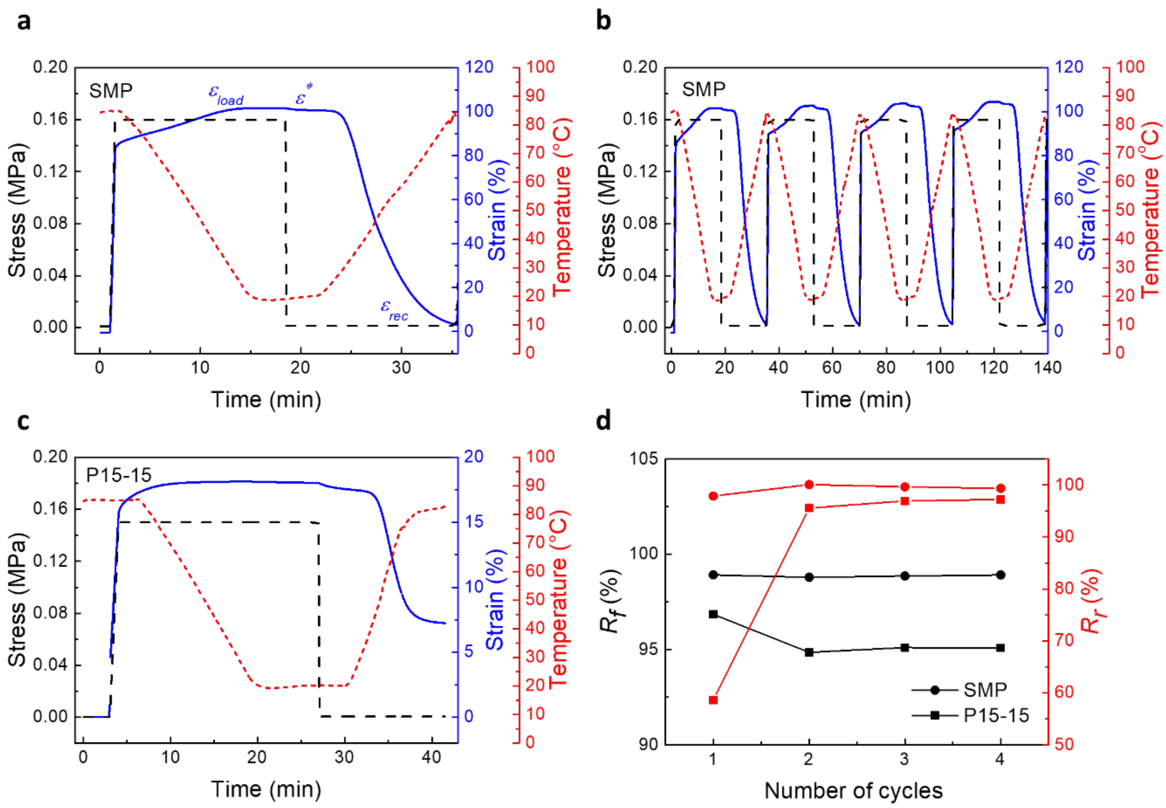

Figure S6. Characterization of shape memory performance of neat SMP and M-SMP (P15-15) using DMA. Temperature, strain, and stress as functions of time for (a) neat SMP in one cycle (b) neat SMP in four cycles and (c) P15-15 in the first cycle. (d) R_f and R_r as functions of cycle number for neat SMP and P15-15. In (a-c), black dashed lines: stress; blue solid lines: strain; red dotted lines: temperature.

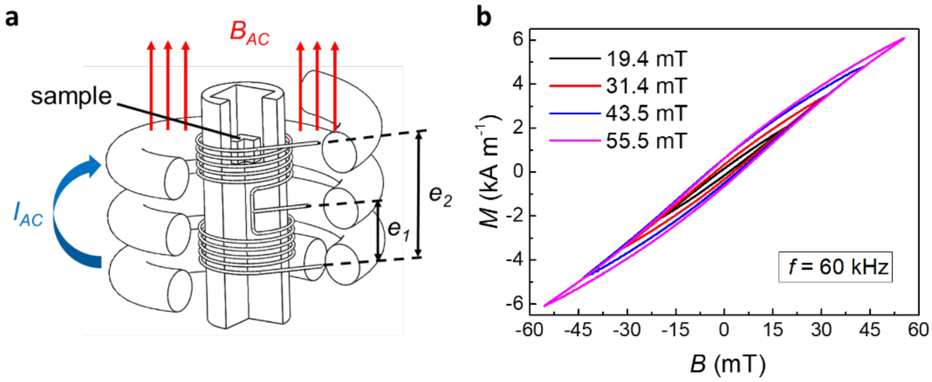

Figure S7. Magnetic inductive heating characterization. (a) Schematic of the experimental setup for measuring high-frequency hysteresis loops. (b) Hysteresis loops of P15-15 under 60 kHz AC magnetic field with different strengths (19.4 mT, 31.4 mT, 43.5 mT, and 55.5 mT).

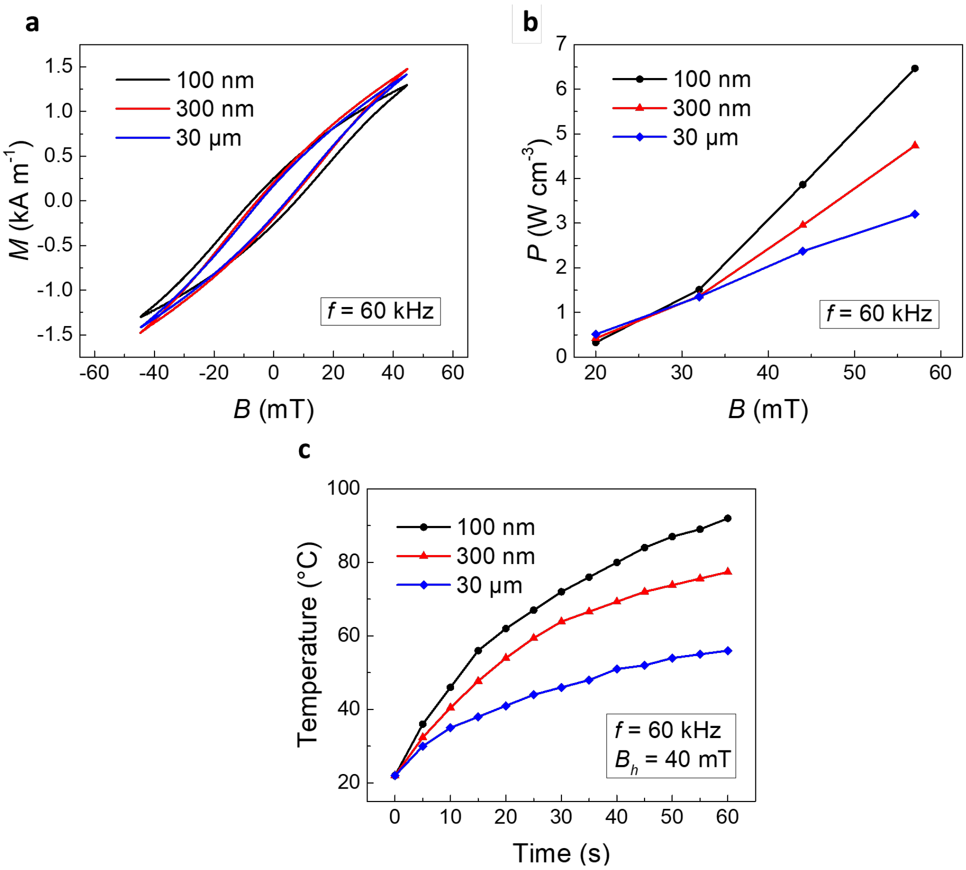

Figure S8. Magnetic inductive heating characterization of P5-5 M-SMPs with different Fe_3O_4 particle sizes (30 µm, 300 nm, and 100 nm) under 60 kHz AC magnetic field. (a) Hysteresis loops of three M-SMPs. (b) Magnetic heating power densities of three M-SMPs under different B_h. (c) Temperature rise curves of three M-SMPs under heating magnetic field of 40 mT.

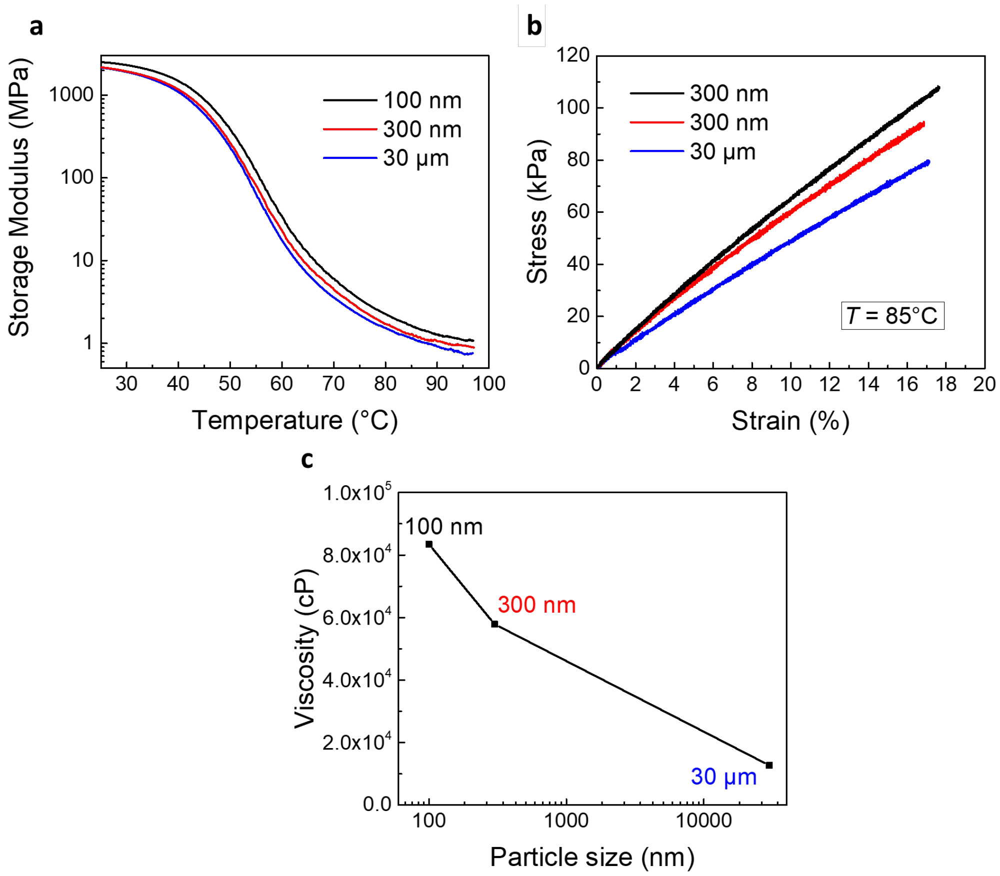

Figure S9. Mechanical characterizations of P5-5 M-SMPs with different Fe_3O_4 particle sizes (30 μm, 300 nm, and 100 nm). (a) Storage modulus versus temperature curves of three M-SMPs. (b) Tensile stress-strain curves of three M-SMPs at 85°C. (c) Viscosity of three M-SMP mixtures.

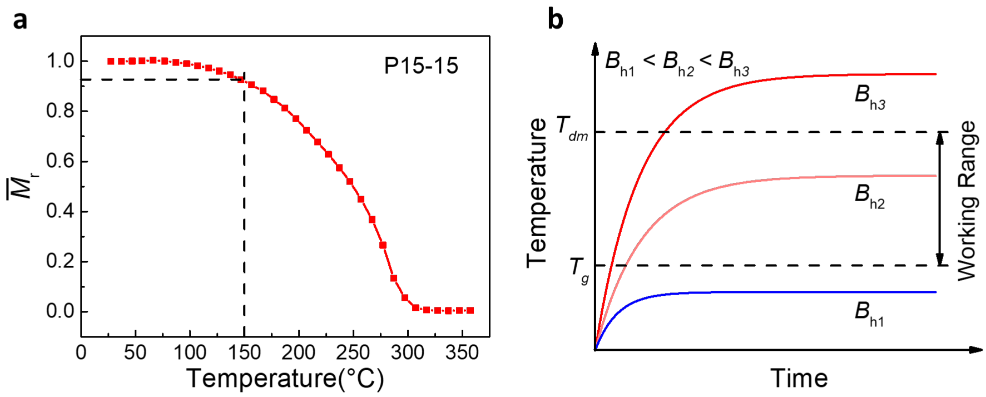

Figure S10. Temperature-dependent demagnetization property curve of P15-15. (a) Influence of temperature on the magnetization of P15-15. At 150ºC, the normalized remnant magnetization $\overline{M_r}$ is approximately 0.91, which can be considered a significant reduction. Therefore, we choose 150ºC as the demagnetization temperature. (b) Temperature-time diagram of inductively heated M-SMP using different heating magnetic fields ($B_{h1}< B_{h2}<B_{h3}$). T_g is the glass transition temperature, and T_{dm} is the demagnetization temperature at which the magnetization of the M-SMP starts to drop significantly. Since it is reasonable to assume that the normalized remnant magnetization should be applied to M-SMPs with different NdFeB loadings, this figure should apply to all M-SMP samples used in this paper.

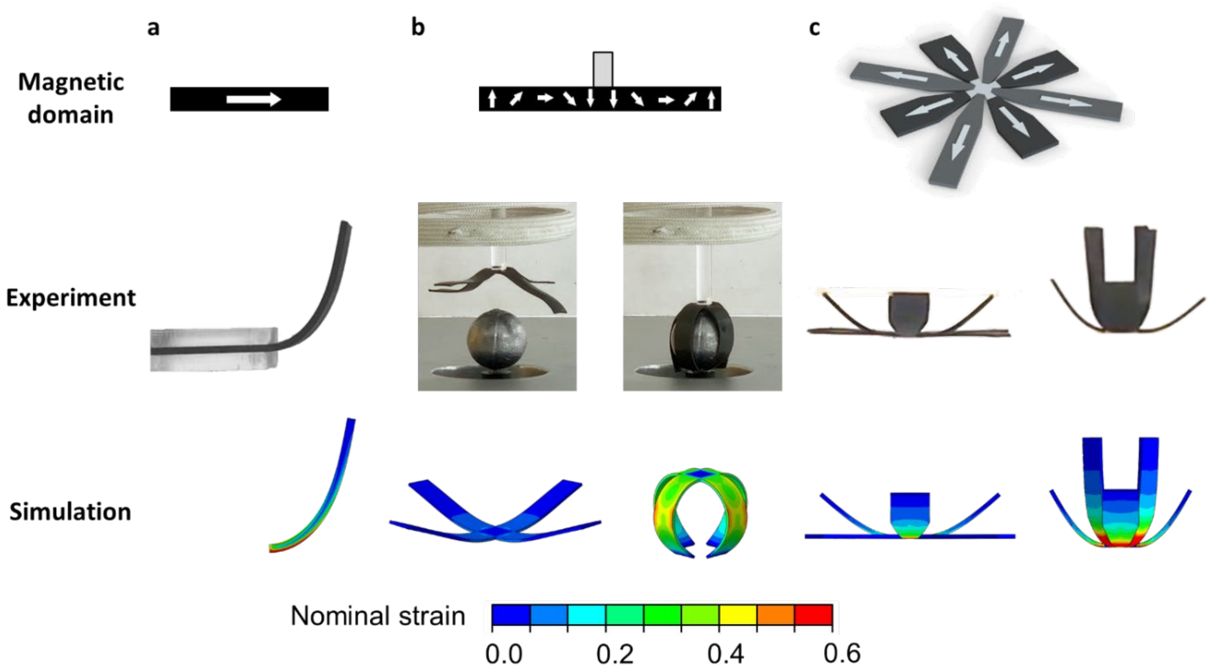

Figure S11. Comparison between experimental results and finite element simulations. (a) Cantilever (Figure 3b). (b) Four-arm M-SMP gripper (Figure 3f). (c) Flower-like structure using P5-15 and P25-15 (Figure 5d).

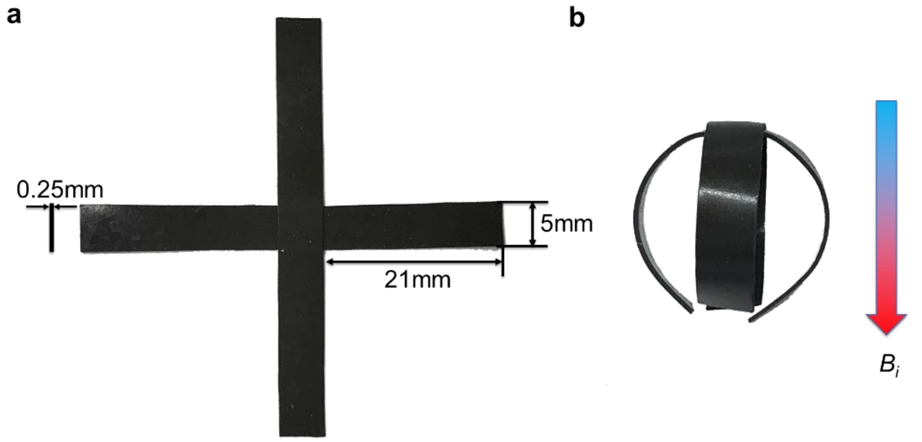

Figure S12. Design and magnetization process of the gripper. (a) Unfolded view of the gripper. (b) Magnetization process of the gripper, B_i indicates the impulse magnetic field.

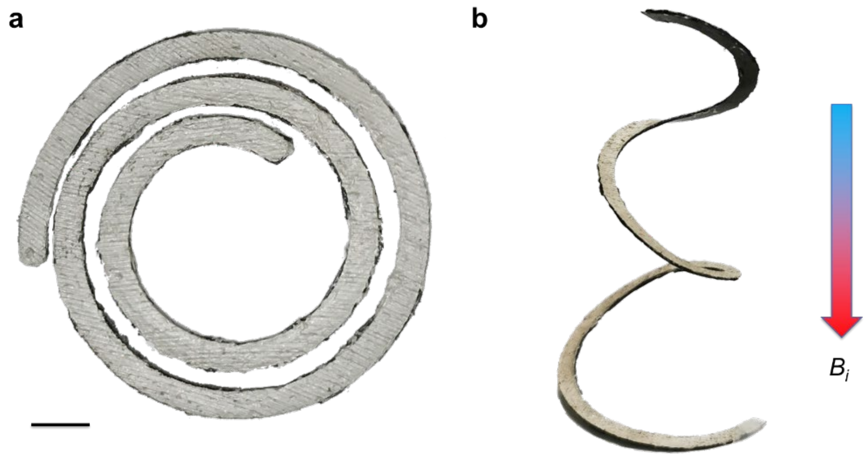

Figure S13. Design and magnetization process of the helical antenna. (a) Unfolded view of the helical antenna. (b) Magnetization process of helix antenna. B_i indicates the impulse magnetic field. Scale bar: 5 mm.

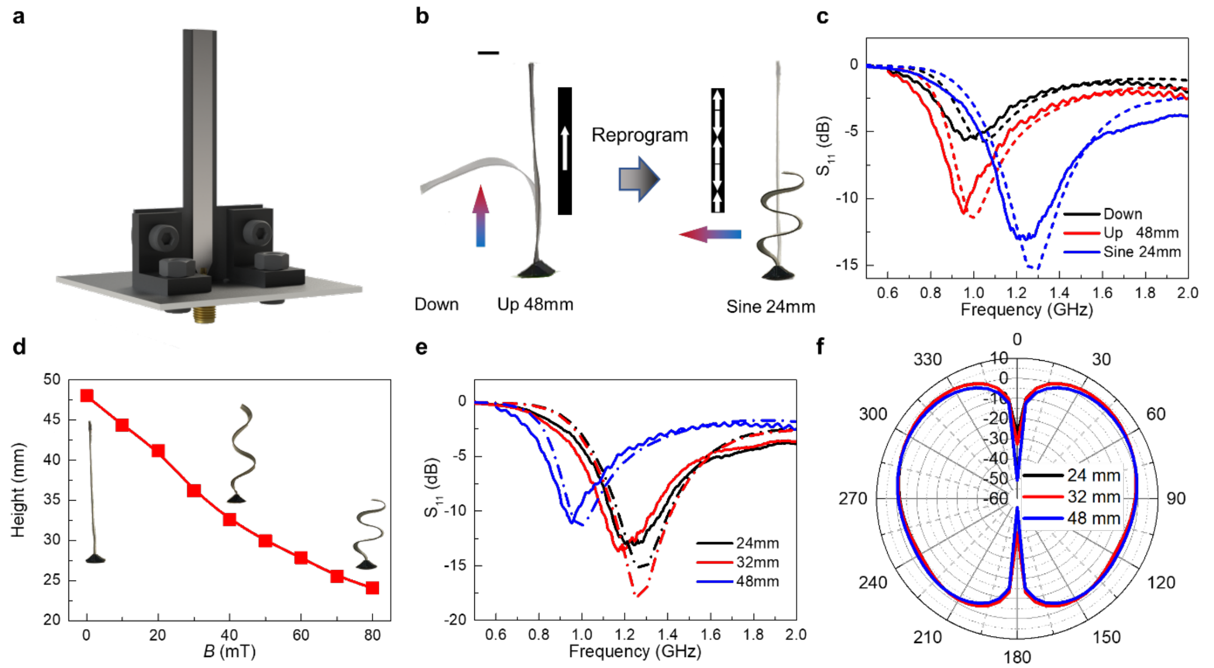

Figure S14. Application of M-SMP as a single-cantilever monopole antenna**.** (a) Schematic of the antenna. (b) Cantilever antenna with two different magnetization profiles by reprogramming. (c) Experimental (solid lines) and simulation (dashed lines) results of the S_{11} spectrum. Characterizations of the cantilever antenna with up and down positions (first magnetization profile). (d) Height versus actuation magnetic field for the sinusoidal antenna (second magnetization profile). (e) Experimental (solid lines) and simulation (dashed lines) results of the S_{11} band at different heights. (f) 2D polar plot of simulated radiation patterns at different heights. Scale bar: 5mm.

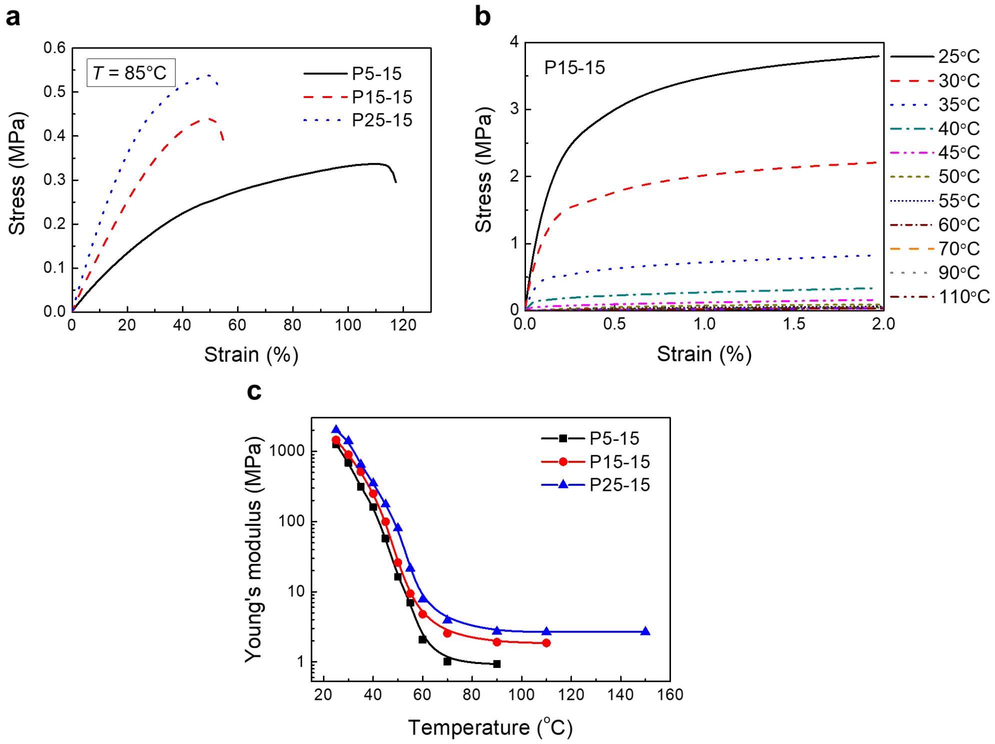

Figure S15. Tensile properties of M-SMPs with different Fe_3O_4 loadings at different temperatures. (a) Comparison of tensile stress-strain curves for three M-SMPs at 85°C. (b) Tensile stress-strain curves of P15-15 at different temperatures with 2% strain. (c) Young's moduli of three M-SMPs as functions of temperature. The strain rate is 0.2 min^{-1}.

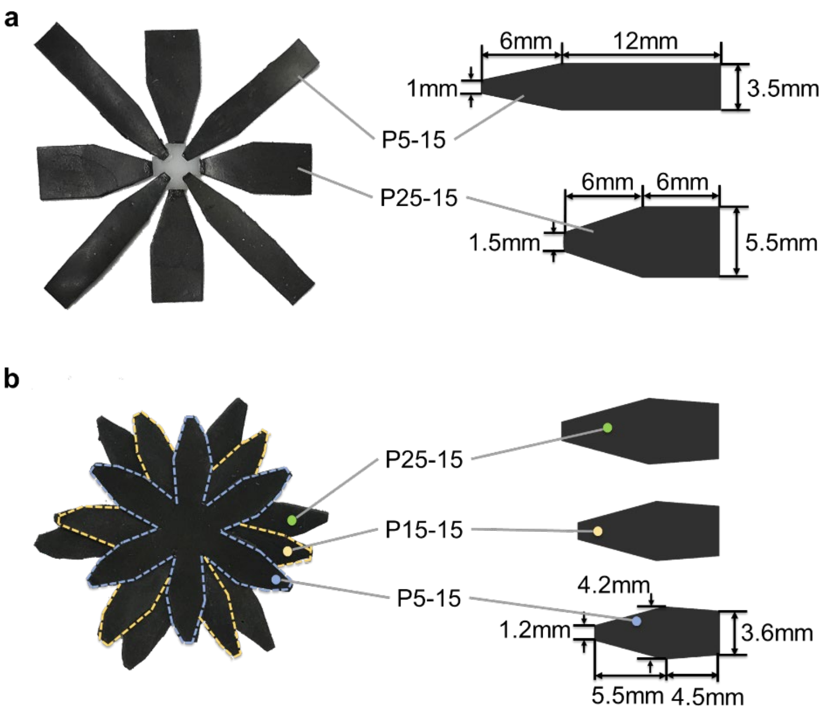

Figure S16. Design and dimensions of the samples used for sequential actuations. (a) Unfolded view and dimensions of the flower sample shown in Figure 5b. (b) Unfolded view and dimensions of the flower sample shown in Video S4. The top, middle, and bottom layers are P5-15, P15-15, and P25-15, respectively. The ratio between the dimensions of P5-15, P15-15, and P25-15 is 0.8: 0.9: 1.

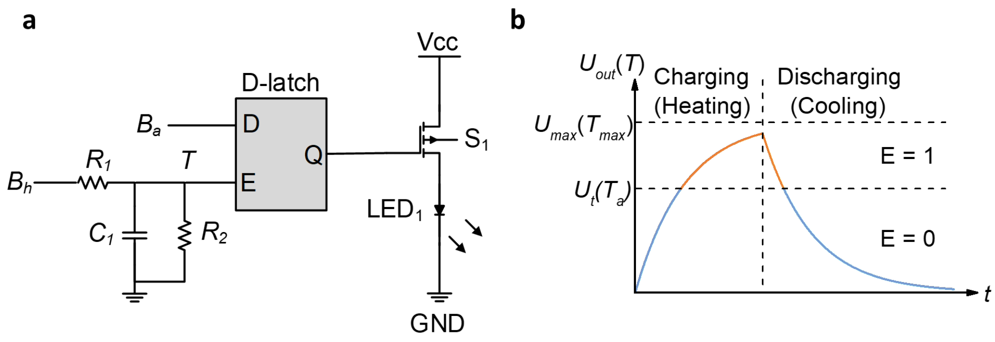

Figure S17. Design of the M-SMP-enabled D-latch system. (a) Schematic of the system. (b) Diagram of the equivalent RC delay circuit. T is the temperature of M-SMP, T_{max} is the maximum temperature that the M-SMP can reach, T_a is the threshold temperature at which the M-SMP can be actuated, U_{in} is the input voltage of the RC delay circuit, U_{out} is the voltage of capacitor C_1, U_{max} is the maximum voltage that the capacitor can reach, and U_t is the threshold voltage at which the input signal can be recognized as high voltage level (Binary 1) by the D-latch. Theoretically, $U_{max} = U_{in} \times R_2 \times (R_1 + R_2)^{-1}$.

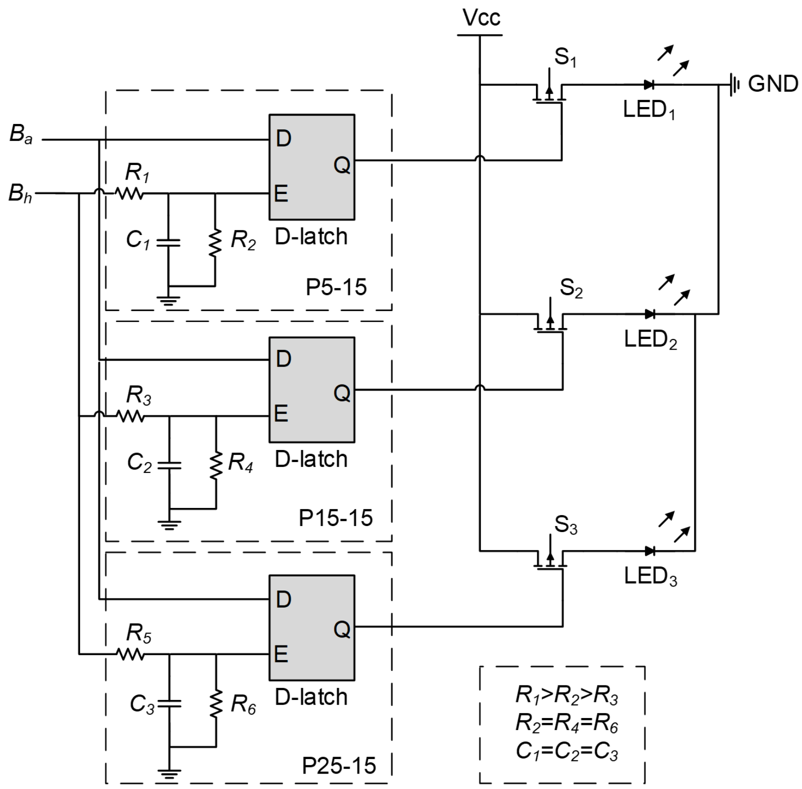

Figure S18. Schematic of the sequential logic circuit using three M-SMPs with different Fe_3O_4 loadings (P5-15, P15-15, and P25-15). *R1>R2>R3* means the time constants of three materials decrease with increasing Fe_3O_4 loadings.

Supplementary Tables and Table Captions

Table S1. Comparison of Soft active materials

Soft active materials	**Stimulus**	**Reversible actuation**	**Rapid actuation**	**Untethered control**	**Reprogramming capability**	**Shape locking**
M-SMP (this work)	Magnetic field & heat	√	√	√	√	√
SMP	Heat	√	×	√	×	√
Hydrogel	Osmotic pressure; PH	√	×	√	×	√
Liquid crystal elastomer	Heat; Light	√	√	√	×	×
Dielectric elastomer	Electric field	√	√	×	×	×
Magnetic elastomer	Magnetic field	√	√	√	√	×

Table S2. Formulation of the matrix resin for the neat SMP.

Diacylate cross-linker	Acrylate monomer			Initiator	Rheology modifier
AUD (wt%)	IOA (wt%)	PA (wt%)	IA (wt%)	AIBN (wt%) [a]	SiO_2 (wt%) [a]
0.7	60.2	30.1	9	0.4	2

[a] Percentage to the weight of acrylates mixture.

Table S3. Formulation for the neat SMP and M-SMPs.

Sample	Resin(vol%)	Fe_3O_4(vol%)	NdFeB(vol%)
SMP	100	0	0
P0-15	85	0	15
P15-0	85	15	0
P3-3	94	3	3
P5-15	80	5	15
P15-15	70	15	15
P25-15	60	25	15

Px-y: x is the Fe_3O_4 volume fraction, **y** is the NdFeB volume fraction.

Table S4. Formulation of the matrix resins for the SMPs with different T_g.

	Diacylate cross-linker	Acrylate monomer			Initiator	Rheology modifier	T_g
	AUD (wt%)	IOA (wt%)	PA (wt%)	IA (wt%)	AIBN (wt%)	SiO_2 (wt%)	(°C)
Sample 1	0.7	9	30.1	60.2	0.4	2	-5.7
Sample 2	0.7	60.2	30.1	9	0.4	2	55
Sample 3	0.7	99.3	0	0	0.4	2	94.9

Table S5. Lifting ratios of current M-SMPs with different particle loadings and different designs

M-SMP	Open state	Actuation	Grabbing	Lifting ratio
P15-15				**105** (Gripper:0.22g Weight: 23.0g)
P3-3				**209** (Gripper:0.11g Weight: 23.0g)
P3-3				**1113** (Gripper:0.10g Weight: 111.3g)

Table S6. Comparison of performance of soft active material grippers in existing studies

Technology	Lifting ratio[a]	Untethered control	Holding w/o constant energy	Reversibility
M-SMP (this work)	1113	√	√	√
Pneumatic actuated elastomer [5]	53[b]	×	√	√
Granular jamming [6]	15.1[c]	×	√	√
Magnetic soft material [7]	N/A[d]	√	×	√
pH-triggered hydrogel [8]	8.3[e]	√	√	√
Bidirectional SMP [9]	3.8[f]	√	√	√
Dielectric actuated SMP [10]	30	×	√	√
SMP w/ controllable curvature [11]	960	√	√	×

[a] Lifting ratio = object weight / gripper weight.

[b] The reported object weight is 300 g. The gripper weight is estimated by the dimension of the gripper and the density of the elastomer.

[c] The ratio is from a review paper of soft robotic grippers [12].

[d] The weight of the gripper and object were not reported. Silicone oil was used as the pneumatic fluid for lifting the object.

[e] The reported object weight and gripper weight are 5 g and 0.6 g, respectively.

[f] The reported object is a penny, whose weight is 2.5 g. The gripper weight is estimated by the dimension of the gripper and the density of the SMP.

Table S7. Input definition of the sequential logic circuit using M-SMPs with different Fe_3O_4 loadings.

Control signal			Input definition		
B_a	Heating time (B_h = 1)	Cooling time (B_h = 0)	I_1	I_2	I_3
0	0	-[a]	0	0	0
1	0	-	1	1	1
0	6	9	1	1	0
1	6	9	0	0	1
0	12	18	1	0	1
1	12	18	0	1	0
0	28	42	0	1	1
1	28	42	1	0	0

[a] "–" means cooling time can be any length.

Table S8. Logic table of the sequential logic circuit using M-SMPs with different Fe_3O_4 loadings.

Input			Output[a,b]		
I_1	I_2	I_3	Q_1	Q_2	Q_3
0	0	0	Latch	Latch	Latch
1	1	1	Latch	Latch	Latch
1	1	0	Latch	Latch	0
0	0	1	Latch	Latch	1
1	0	1	Latch	0	0
0	1	0	Latch	1	1
0	1	1	0	0	0
1	0	0	1	1	1

[a] Subscripts 1, 2, 3 stand for sample P5-15, P15-15, P25-15, respectively.
[b] Binary 1 means the LED is on, Binary 0 means the LED is off;

According to Table S4, logical equations can be derived as follows:

$$\begin{cases} Q_1^{n+1} = (I_1I_2I_3 + \overline{I_1I_2I_3})Q_1^n + ((\overline{I_1I_2I_3 + \overline{\overline{I_1I_2I_3}}})((I_2I_3 + \overline{I_2I_3})Q_1^n + (I_1I_3 + \overline{I_1I_3})Q_1^n + (I_1I_2 + \overline{I_1I_2})I_3) \\ Q_2^{n+1} = (I_1I_2I_3 + \overline{I_1I_2I_3})Q_2^n + ((\overline{I_1I_2I_3 + \overline{\overline{I_1I_2I_3}}})((I_2I_3 + \overline{I_2I_3})Q_2^n + (I_1I_3 + \overline{I_1I_3})I_2 + (I_1I_2 + \overline{I_1I_2})I_3) \\ Q_3^{n+1} = (I_1I_2I_3 + \overline{I_1I_2I_3})Q_3^n + ((\overline{I_1I_2I_3 + \overline{\overline{I_1I_2I_3}}})((I_2I_3 + \overline{I_2I_3})I_1 + (I_1I_3 + \overline{I_1I_3})I_2 + (I_1I_2 + \overline{I_1I_2})I_3) \end{cases} \quad \text{, (S6)}$$

where Q_i^{n+1} is the next LED state of Q_i^n, i = 1, 2, and 3.

Supplementary Video Captions

Video S1:

Magnetic actuation and shape-locking of a 1-D cantilever (Figure 3).

Video S2:

Four-arm M-SMP gripper lifting a lead ball by shape-locking (Figure 3).

Video S3:

Magnetic actuation and shape-locking of a reconfigurable antenna (helical design) (Figure 4).

Video S4:

Magnetic actuation and shape-locking of a reconfigurable antenna (sinusoidal design) (Figure S10).

Video S5:

Sequential actuation and shape-locking of a flower-like M-SMP structure (Figure 5).

Video S6:

Flower blooming-inspired sequential shape-transformation.

Video S7:

Sequential logic circuit using M-SMPs (Figure 5).

References

[1] V. Connord, B. Mehdaoui, R. Tan, J. Carrey, M. Respaud, *Rev. Sci. Instrum.* **2014**, *85*, 093904.

[2] M. Y. Razzaq, M. Anhalt, L. Frormann, B. Weidenfeller, *Mater. Sci. Eng., A* **2007**, *444*, 227.

[3] a) S. Yao, X. Liu, J. Gibson, S. V. Georgakopoulos, *2015 IEEE International Symposium on Antennas and Propagation & USNC/URSI National Radio Science Meeting* **2015**; b) J. M. Kovitz, H. Rajagopalan, Y. Rahmat-Samii, *IEEE Trans. Antennas Propag.* **2015**, *63*, 2497.

[4] R. Zhao, Y. Kim, S. A. Chester, P. Sharma, X. Zhao, *J. Mech. Phys. Solids* **2019**, *124*, 244.

[5] F. Ilievski, A. D. Mazzeo, R. F. Shepherd, X. Chen, G. M. Whitesides, *Angew. Chem. Int. Ed.* **2011**, *50*, 1890.

[6] J. Amend, N. Cheng, S. Fakhouri, B. Culley, *Soft robotics* **2016**, *3*, 213.

[7] T. Xu, J. Zhang, M. Salehizadeh, O. Onaizah, E. Diller, *Science Robotics* **2019**, *4*, eaav4494.

[8] J. Duan, X. Liang, K. Zhu, J. Guo, L. Zhang, *Soft Matter* **2017**, *13*, 345.

[9] M. Behl, K. Kratz, J. Zotzmann, U. Nöchel, A. Lendlein, *Adv. Mater.* **2013**, *25*, 4466.

[10] D. McCoul, S. Rosset, N. Besse, H. Shea, *Smart Mater. Struct.* **2016**, *26*, 025015.

[11] A. M. Hubbard, R. W. Mailen, M. A. Zikry, M. D. Dickey, J. Genzer, *Soft Matter* **2017**, *13*, 2299.

[12] J. Shintake, V. Cacucciolo, D. Floreano, H. Shea, *Adv. Mater.* **2018**, *30*, 1707035.